Lingfeng Gao
Dept. of Mechanical Engineering,
State Univ. of New York at Stony Brook,
Stony Brook, NY 11794, USA
email: lingfeng.gao@stonybrook.edu

Xiaoping Zhu
Dept. of Applied Mathematics & Statistics,
State Univ. of New York at Stony Brook,
Stony Brook, NY 11794, USA
email: xz349@scarletmail.rutgers.edu

Masato Tanaka
Toyota Research Institute of North
America, Ann Arbor, MI 48105, USA
(Current affiliation: Toyota Central R&D
Labs., Inc., 41-1, Yokomichi, Nagakute,
Aichi, 480-1192, JAPAN)
email: tanamasa@mosk.tytlabs.co.jp

Yuyang Song
Toyota Research Institute of North
America, Ann Arbor, MI 48105, USA
email: yuyang.song@toyota.com

Yuqing Zhou
Toyota Research Institute of North
America, Ann Arbor, MI 48105, USA
email: yuqing.zhou@toyota.com

Xianfeng David Gu
Dept. of Computer Science,
Dept. of Applied Mathematics & Statistics,
State Univ. of New York at Stony Brook,
Stony Brook, NY 11794, USA
email: gu@cs.stonybrook.edu

Shikui Chen[1]
Dept. of Mechanical Engineering,
State Univ. of New York at Stony Brook,
Stony Brook, NY 11794 USA
email: shikui.chen@stonybrook.edu

Geometry-Driven Design of Morphable Surface Structures Using Topology Optimization and Circle Packing

This paper introduces a new computational framework for modeling and designing morphable surface structures based on an integrated approach that leverages circle packing for surface representation, conformal mapping to link local and global kinematics, and topology optimization for actuator design. The framework utilizes a unique strategy of employing optimized compliant actuators as the basic building blocks of the morphable surface. These actuators, designed as circular elements capable of modifying their radius and curvature, are optimized using level-set topology optimization, considering both kinematic performance and structural stiffness. Circle packing is employed to represent the surface geometry, while conformal mapping guides the kinematic analysis, ensuring alignment between local actuator motions and desired global surface transformations. The design process involves mapping optimized component designs back onto the circle packing representation, facilitating coordinated control and achieving harmony between local and global geometries. This leads to efficient actuation and enables precise control over the surface morphology. The effectiveness of the proposed framework is demonstrated through two numerical examples, showcasing its capability to design complex, morphable surfaces with potential applications in fields requiring dynamic shape adaptation.

Keywords: Morphable Structures. Circle Packing. Conformal Mapping. Compliant Mechanisms. Topology Optimization. Level Set Method. Differential Geometry.

1 INTRODUCTION

Morphable structures capable of transforming into various shapes on demand have garnered significant attention in recent years due to their wide-ranging applications in fields such as soft robotics [1–3], deployable structures in aerospace engineering [4], and adaptive automotive systems [5]. The ability to design structures that morph predictably and controllably between target geometries enables novel functionalities and enhances system versatility. However, the rational design and precise control of morphable structures pose significant challenges due to the complex interplay between material properties, structural mechanics, and desired shape transformations.

To address these challenges, researchers have increasingly turned to computational methods for the systematic design of these complex systems. Topology optimization has emerged as a powerful tool for designing structures with optimized material distribution to achieve desired performance objectives [6,7], enabling the creation of lightweight, high-performance, and multifunctional structures [8,9]. In the context of morphable structures, topology optimization has been leveraged to design compliant mechanisms and shape-morphing systems. Contemporary design approaches for mechanical compliant mechanisms can be broadly classified into two categories: kinematics-based methods and structural optimization-based methods. The kinematics-based approach, as represented by Howell [10] and Smith [11], is rooted in the concept of flexible linkages [12–14]. In this framework, compliant mechanisms are modeled using pseudo-rigid bodies connected by notched flexible hinges, where motion is achieved through the bending deformation of these notched regions. The second category, structural optimization-based methods, leverages advanced computational techniques to achieve optimal designs. These include the ground structure method[15], the homogenization method [16], the solid isotropic material with penalization (SIMP) method [17], and level-set-based methods[18,19]. Recent advancements in this category include innovative approaches such as the flexible

[1]Corresponding Author.
Version 1.18, September 7, 2025

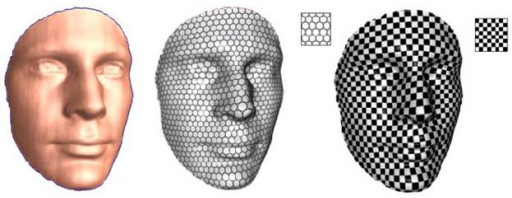

Fig. 1 PROPERTIES OF CONFORMAL MAPPING: LOCAL SHAPES (SQUARES AND CIRCLES) ARE PRESERVED IN THE TRANSFORMATION FROM THE PLANE TO THE SURFACE [34,35].

building block method [20], the unit cell approach [21], the radial basis function (RBF) level set method [22], and the cardinal basis function (CBF) level set method [23].

Designing and modeling shape-morphing structures pose significant challenges due to complex morphing modes, scalability, and conformal geometries. Predicting deformation at both the unit cell and surface levels is often uncertain, with additional difficulties in controlling target geometries, ensuring path dependence, and achieving reversibility. Approaches such as auxetic morphing structures for mechanical metamaterials [24] and shape memory polymers as smart materials [25] have been explored. However, auxetic structures face limitations, including difficulties in morphing control, pattern design, and integration across scales. However, existing approaches often struggle to simultaneously maintain precise local geometries and overall shape integrity during the morphing process, limiting their applicability to more complex target geometries [26–29].

To address these challenges, we intorduce a new approach that seamlessly integrates computational conformal geometry with topology optimization, resulting in an effective framework for designing morphable surface structures. Our approach leverages circle packing, a technique for discretely representing surfaces using tangent circles, to model the target morphing behavior. Conformal mapping is then employed to transform the circle-packed surface between 2D and 3D configurations while preserving angle measurements [30,31]. This mapping technique ensures that local geometries are preserved, guaranteeing the integrity of local geometries even during significant global shape changes. By recasting the morphable surface design problem as the design of an interconnected network of circular compliant mechanisms, we can apply topology optimization to generate realistic structures capable of morphing into the desired geometries [32,33].

This work makes two main contributions:

First, we introduce a conformal geometry-driven approach for modeling and designing the morphing of surface structures. This approach uses circle packing to represent the surface and uses discrete Ricci flow to guide its transformation. This mathematical framework provides a reliable way to define and achieve desired morphing behaviors while preserving the shape integrity of the structure.

The use of circle packing offers several advantages for the kinematic modeling of morphable surface structures. It enables an accurate representation of the surface geometry, which is crucial for shape modeling. Conformal mapping, used in conjunction with circle packing, preserves angles between curves on the surface, ensuring that the overall shape is maintained throughout the morphing process. Additionally, Ricci flow refines the surface shape and simulates its temporal evolution, facilitating the creation of highly realistic and dynamic models of morphable surface structures. This methodology proves particularly beneficial for the physical realization of morphable structures using topology optimization, where maintaining both local and overall shape integrity during morphing is imperative for correct structural functionality.

Second, we develop a pipeline for integrating this conformal geometric modeling with topology optimization to automatically generate designs for morphable surface structures that can be fabricated as single-piece compliant mechanisms. The coupling of conformal geometry and topology optimization opens up new possibilities for designing complex and precise morphable structures.

By using circle packing, we can translate the overall morphing of the surface into local changes in the radii of the circles. This transforms the complex problem of morphing surface design into a simpler problem of designing circular actuators that can expand and contract to change the shape of the surface. After optimizing the design of a single-piece compliant mechanism using topology optimization, we assemble a circular actuator by revolving this mechanism around its central axis. This circular actuator is then mapped to a circle packing pattern, allowing us to adjust the radii of the circles and morph the overall surface shape. This approach, using circular actuators to modify the circle packing pattern, makes the surface structure more adaptable and deformable. We have performed two numerical simulations to demonstrate the effectiveness of our method.

The rest of the paper is organized as follows: Section 2 provides the necessary mathematical background on circle packing and conformal geometry. Section 3 explains how we combine conformal geometry with topology optimization and formulate the design problem. Section 4 describes our topology optimization method and sensitivity analysis. Section 5 presents numerical examples that demonstrate the effectiveness of our approach. Finally, Section 6 discusses the implications of our work and suggest directions for future research.

2 CIRCLE PACKING THEORY

Circle packing is a technique used in computational conformal geometry to represent surfaces using a collection of circles that touch each other in a specific way. The way these circles touch, or their tangency relationships, is determined by the shape of the surface being represented **??**[36,37]. Circle packing's ability to capture detailed geometric information and maintain its structure under conformal transformations makes it a valuable tool for modeling surface morphing. By leveraging the properties of circle packing, we can develop effective methods for modeling and controlling the morphing of surface structures. In this section, we introduce the mathematical foundations of circle packing and its application in representing and manipulating surfaces.

2.1 Koebe-Andreev-Thurston Theorem. The Koebe-Andreev-Thurston Theorem (KAT Theorem) [38] is the fundamental theorem in the circle packing theory. It states that for a finite maximal planar graph G, there exists a circle packing whose tangency graph is isomorphic to G and is unique, up to Möbius transformations and reflections in lines. As shown in Fig. 2, given a planar graph, one can compute a circle packing, which associates each vertex with a circle (vertex circle), and each face with a circle (face circle), such that

1. For every edge, the two vertex circles associated with the end vertices are tangential to each other;
2. For every edge, the two face circles associated with the adjacent faces are tangential to each other;
3. For every edge, the two face circles and the two vertex circles intersect at the same point.
4. Within each face, the face circle is tangential to the edges, and orthogonal to all the vertex circles;

The KAT Theorem established a connection between a finite graph's topology and geometric realization. Furthermore, it is closely related to the conformal mapping between planar domains. The Riemann mapping theorem states that there is a conformal map from one disk to the other for any two topological disks in the plane. However, it is not easy to construct an explicit conformal mapping between two given domains.

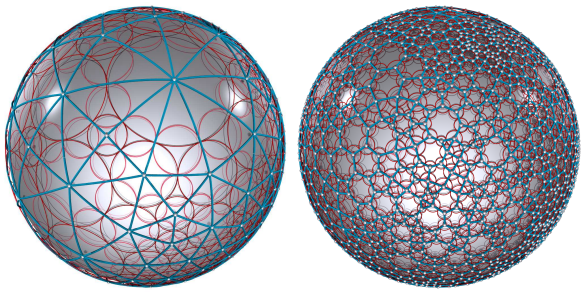

Fig. 2 Koebe-Andreev-Thurston circle packing theorem.

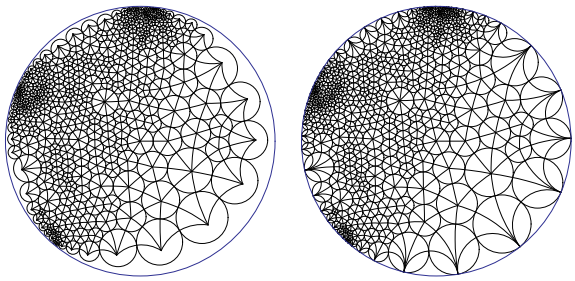

Fig. 3 DISCRETE CONFORMAL MAPPINGS.

In 1985, Thurston proposed using circle packings to approximate conformal mappings. He suggested filling a domain Ω with a hexagonal tessellation of circles, each of small radius r, and forming a planar graph G from the intersection graph of those circles. The KAT theorem guarantees a circle packing, with the outermost circle as the unit circle, whose tangency graph is isomorphic to G. The resulting discrete conformal mapping is the piecewise linear mapping that preserves the combinatorial structure of G.

As shown in Figure 3, we compute a triangulation of the domain Ω with a circle packing in the left frame, then deform the circle packing to fill the unit disk in the right frame, this gives a piecewise linear mapping f_0. By subdividing the triangulation and repeating the process, we get f_1. In the same way, we can get a sequence of those discrete conformal mappings f_n sending the interior of a region Ω to the unit disk D. Thurston conjectured that as the radius of the tessellation goes to zero, the discrete conformal mappings f_n will converge to the Riemann mapping. This conjecture was confirmed by Rodin and Sullivan in 1987 [39].

2.2 Discrete Ricci Flow and Circle Packing. However, there is no natural analogy for the circle packings on general curved surfaces. Ricci flow on surfaces was first introduced by Hamilton in [40]. Chow and Luo discovered the relations between the Ricci flow and the circle packings and established the theoretical foundation for discrete Ricci flow in [41] , where the existence and convergence of the discrete Ricci flow were established.

Consider M as a two-dimensional, connected, orientable surface, and T is a simplicial *triangulation* of M. Let $V(T), E(T), andF(T)$ be the set of vertices, edges, and triangles of T, respectively. Furthermore, when M is equipped with a Riemannian metric, T is called a *geodesic triangulation* if every edge in T is a geodesic arc.

Given a triangulation T, if an edge length $l \in \mathbb{R}_{>0}^{E(T)}$ satisfies the triangle inequalities, we can construct a Euclidean polyhedral surface (T, l) by isometrically gluing the Euclidean triangles with the edge lengths defined by l along the pairs of edges. Notice that a Euclidean polyhedral surface exhibits a piecewise Euclidean metric, for a vertex in $V(T)$ could be a singular cone point, and the Gaussian curvature is constant 0 at any point not in $V(T)$.

Given $(T, l)_E$, let θ_{jk}^i be the inner angle at the vertex i in the triangle $\triangle ijk$. The *discrete curvature* K_i at the vertex $i \in V(T)$ is defined as

$$K_i = 2\pi - \sum_{jk \in E : \triangle ijk \in F} \theta_{jk}^i \tag{1}$$

A piecewise Euclidean metric is globally flat if and only if $K_i = 0$ for every vertex $i \in V(T)$.

In practice, the objects we study are polyhedral surfaces. Figure 4 shows how the polyhedral surfaces relate to circle packings.

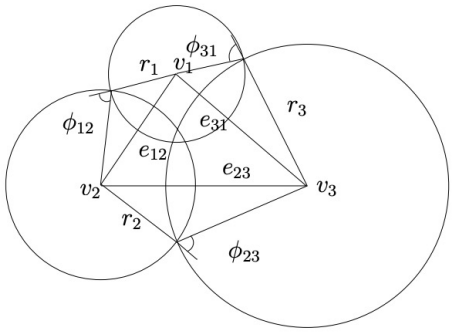

Fig. 4 CIRCLE PACKING FOR A METRIC: Triangle $[v_1, v_2, v_3]$ has vertices v_1, v_2, v_3, and edges e_{12}, e_{23}, e_{31}. Three circles centered at v_1, v_2, and v_3, with radii r_1, r_2 and r_3 intersect one another, with intersection angles of Φ_{12}, Φ_{23} and Φ_{31}, which are the weights associated with the edges. The edge lengths of the triangle are determined by r_i and Φ_{ij} by the cosine law.

Change infinitesimal circles to circles with finite radii, and each circle is centered at a vertex like a cone, the radius is denoted as γ_i at vertex v_i, and an edge has two vertices, the two circles intersect each other with an intersection angle, the angle is denoted as Φ_{ij} for edge e_{ij}, and called the weight.

Definition 1. *A mesh with circle packing (M, Γ, Φ), where M is the topological triangulation (connectivity), $\Gamma = \{\gamma_i, v_i \in V\}$ are the vertex radii, $\Phi = \{\Phi_{ij}, e_{ij} \in E\}$ are the angles associated with each edge. A discrete conformal mapping $\tau : (M, \Gamma, \Phi) \to (M, \bar{\Gamma}, \Phi)$ only changes the vertex radii Γ, but preserves the intersection angles Φ.*

In geometric modeling applications, meshes are typically embedded in $\mathbb{R}^3$ with the metrics induced from the embedding. We can find the optimal weight Φ with initial circle radii Γ, such that the circle packing metric (M, Φ, Γ) is as close as possible to the Euclidean metric in the least square sense. Namely, we want to

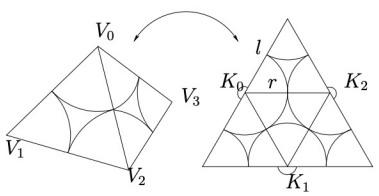

Fig. 5 CIRCLE PACKING AND CURVATURE: For a canonical tetrahedron, the edges lengths are all $l = 1.0$, and the radius at each vertex is $r = 0.5$. The curvature on each vertex equals to $K_i = \pi$. The weights on all edges are $\Phi = 0$.

determine (M, Φ, Γ) by minimizing the following functional

$$\min_{\Gamma,\Phi} \sum_{e_{ij}\in E} |l_{ij} - \bar{l}_{ij}|^2 \tag{2}$$

where $\bar{l}_{ij}$ is the edge length of e_{ij} in $\mathbb{R}^3$.

Then we could utilize the discrete Ricci flow to yield a virtual circle packing realizing the desired curvature.

Definition 2 (Discrete Ricci flow)**.** *The discrete Ricci flow is defined as*

$$\frac{d\gamma_i}{dt} = (\bar{K}_i - K_i)\gamma_i, \tag{3}$$

where $\bar{K}_i$ is the desired discrete curvature.

The discrete Ricci flow is a powerful tool for manipulating circle packings and transforming surface geometries. It operates by adjusting the radii of the circles in a packing based on the difference between their current and target curvatures. The Ricci flow equation (Eq. 3) describes how the radius of each circle evolves over time, with the goal of converging to a packing that realizes the desired curvature distribution. Thurston [42] proved that if the target curvatures satisfy special inequality constraints, then the desired circle radii exist.

2.3 Isometric Embedding. Suppose M is a genus zero closed surface with a Riemannian metric $\mathbf{g}$, such that the Gaussian curvature is positive everywhere, then the classical Weyl Embedding theorem [43] claims that the surface can be isometrically embedded in $\mathbb{R}^3$, and embedding is unique upto a rigid motion. The theorem has been generalized to the discrete setting:

Theorem 1 (Alexandrov [44])**.** *Let M be a sphere with a convex polyhedral metric. Then there exists a convex polytope $P \subset \mathbb{R}^3$ such that the boundary of P is isometric to M. Moreover, P is unique up to a rigid motion.*

A similar isometric embedding theorem holds for convex cap, namely a topological disk with a positive curvature metric [45],

Theorem 2 (Alexandrov Convex Cap)**.** *Let D be a disk with a convex Euclidean polyhedral metric. Then there exists a convex cap $C \subset \mathbb{R}^3$ with the upper boundary isometric to D. Besides, C is unique up to a rigid motion.*

Figure 6 shows the isometric embedding theorems of positive curvature polyhedral metrics.

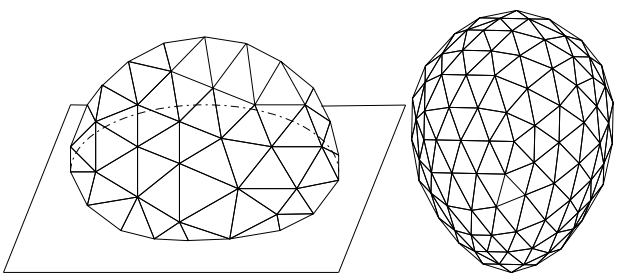

Fig. 6 Alexandrov convex cap theorem (left) and Alexandrov Convex polytope theorem (right).

2.4 Deformation for Surfaces via Circle Packings. As discussed in the last section, given an initial circle packing and the desired curvature for the target metric. We can achieve the target metric through the discrete Ricci flow.

Then Alexandrov convex polyhedron theorem [44] ensures that if the desired curvature at each vertex is positive and the initial circle packing lies on the plane, it is possible to linearly interpolate the curvature to determine the curvature at intermediate steps. Furthermore, the circle packings for those intermediate steps could also be achieved through the discrete Ricci flow. This enables us to outline a deformation process from the initial shape to the target shape via circle packing.

For non-convex target shapes, no theoretical guarantee ensures that the shape at intermediate steps could be embedded in $\mathbb{R}^3$. However, satisfactory results can still be achieved, provided the initial and target shapes are small.

3 DESIGN OF MORPHABLE SURFACES STRUCTURE

3.1 Idea of Design Morphable Surfaces Structure. The morphable surface structure undergoes deformation from a flat panel to a surface (e.g., a hemisphere), causing simultaneous changes in the radii of individual circles. Circle-packing algorithms yield accurate and precise data for each circle during this transformation. Leveraging this radius data, we aim to devise a mechanism capable of morphing in accordance with the data and adjusting the radii accordingly. However, to achieve this complex transformation, we need a mechanism that not only adjusts the radii of individual circular units but also induces curvature changes within them. This is because a physical surface, unlike its mathematical representation, has a thickness and requires bending to achieve the target 3D shape. The paper addresses this by designing actuators that can not only change their radius but also induce curvature.

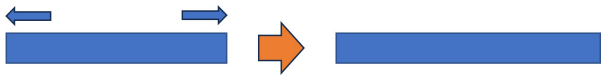

Fig. 7 EXPANSION IN RADIUS.

Achieving radius changes in a single circular actuator is conceptually straightforward. Illustrated in Figure 7, the fundamental concept involves an expansion and pulley mechanism capable of altering its size while preserving its circular form. This principle finds application in machine gearing adjustments, where dynamic modulation of the pulley radius facilitates changes in gear ratio. The expansion and pulley actuator smoothly adjusts the radius by harnessing motive power, which can be supplied by a motor or similar device.

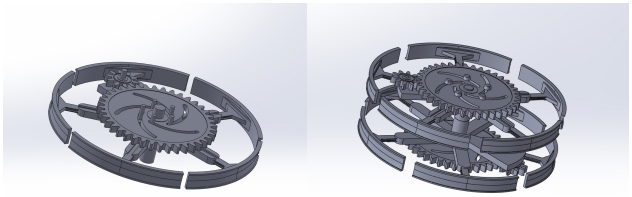

Fig. 8 SINGLE/DOUBLE LAYER OF EXPANSION AND PULLY MECHANISM.

Achieving curvature changes in a single circular actuator presents a significant challenge, as it involves bending the mechanism to approximate the target curvature. Our innovative approach to achieving curvature alterations and radius changes involves incorporating an additional layer into the mechanism. As depicted in

Figure 9, the upper layer of the mechanism expands over a greater distance than the lower layer, resulting in a disparity in length between the two layers. This length difference generates curvature when the mechanism comes into contact with another surface. Building upon this concept, we have developed a novel mechanism termed the double expansion and pulley mechanism, as illustrated in Figure 8

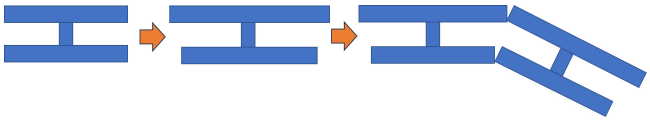

Fig. 9 EXPANSION IN RADIUS AND CURVATURE.

The double expansion and pulley mechanism in Figure 9 consists of two concentric circular layers connected by a series of radial spokes. Each layer comprises a flexible material that can expand or contract in response to an applied force. The outer layer has a slightly larger radius than the inner layer, allowing for differential expansion. The radial spokes ensure the layers maintain their circular shape during expansion and contraction.

To actuate the mechanism, a set of pulleys and cables are employed. The cables are attached to the outer edge of each layer and routed through the pulleys, which are mounted on a fixed frame surrounding the mechanism. By selectively pulling on the cables, the outer layer can expand more than the inner layer, causing the mechanism to bend and assume a curved shape. The curvature of the mechanism can be controlled by adjusting the relative expansion of the two layers. At the same time, the overall radius of the mechanism can be changed by expanding or contracting both layers simultaneously.

Fig. 10 THE KEY IDEA OF THE DOUBLE LAYER MECHANISM AND ITS IMPACT ON THE OVERALL STRUCTURE CURVATURE WHEN MORPHING FROM A PANEL TO A HEMISPHERE.

The double expansion and pulley mechanism offers several advantages over alternative designs. First, by using flexible materials and a simple actuation scheme, the mechanism can achieve smooth and controllable curvature changes without the need for complex hinges or joints. Second, the use of concentric layers allows for independent control of radius and curvature, enabling a wide range of target shapes to be realized. Finally, the mechanism can be easily scaled up or down to suit different application requirements, from small-scale soft robotic components to large-scale adaptive structures.

In the context of morphable surface design, the double expansion and pulley mechanism serve as a key building block for realizing the target curvature distributions prescribed by the circle packing-based surface representation. Complex surface geometries can be achieved by integrating multiple instances of this mechanism into a larger structure and coordinating their actuation. The precise control afforded by the mechanism enables the realization of smooth, continuous shape transformations, as required for many morphable surface applications.

3.2 Rigid Body Mechanism v.s. Compliant Mechanism. Rigid body mechanisms have versatile engineering applications

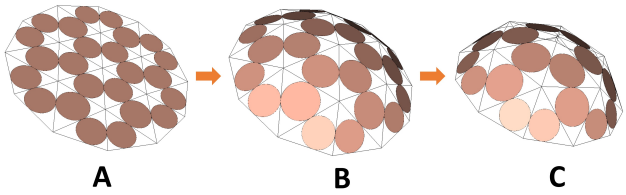

Fig. 11 CIRCLE PACKING SURFACES FROM FLAT TO HEMISPHERE. (a) initial flat plane with uniform circle radii, (b) intermediate state during Ricci flow with partially adjusted radii, and (c) final deformed semi-spherical surface with target curvatures realized.

and find widespread use in manufacturing, robotics, automotive, aerospace, mechanical engineering, and other fields. Their primary advantage lies in their ability to transmit forces and motion through discrete components connected by joints, maintaining structural integrity without deformation. However, when applied to our expansion and pulley system, this traditional approach presents challenges. While such mechanisms can achieve the desired radial expansion and curvature morphing, the complexity of multiple interconnected parts increases the risk of structural instability, particularly through buckling and mechanical failure.

Compliant mechanisms offer an alternative solution that addresses these limitations. By integrating flexibility into their single-piece construction, these mechanisms achieve the desired motion through controlled elastic deformation rather than rigid joints. This approach brings multiple benefits: the structures can be lighter, more compact and adaptable, and simpler to design and manufacture, particularly through modern 3D printing techniques. In our application, using compliant mechanisms for the circular actuators not only simplifies the overall system but also enhances its structural stability and reliability.

3.3 Designing the Morphable Surface Structure Using Circle Packing and Topology Optimization. While circle packing algorithms excel at providing precise mathematical data about circle configurations - specifically their radii and spatial coordinates - they address only part of our design challenge. Traditional circle-packing approaches treat circles as purely geometric entities, focusing solely on their radial dimensions and relative positions. However, in developing practical mechanical systems, we must consider additional physical characteristics that these mathematical models overlook. Specifically, the thickness of the structural elements and their ability to generate controlled curvature become crucial design parameters. This creates a fundamental engineering challenge: how to translate a mathematically elegant circle-packing solution into a physical mechanism that can not only achieve the prescribed radial transformations but also generate and maintain specific curvature profiles throughout its deformation. Our approach bridges this gap between geometric theory and mechanical implementation by developing mechanisms that simultaneously control both radial expansion and surface curvature.

The transformation from a flat panel to a hemispherical configuration provides an illustrative example of these design complexities. To achieve this morphing behavior, we classify the circular elements into three distinct categories based on their radial expansion rates during transformation. As shown in Figure 12, these categories are color-coded: green elements exhibit the highest rate of radial expansion, yellow elements demonstrate intermediate expansion and blue elements show the lowest rate of change. This strategic categorization enables precise control over the local deformation necessary to achieve the global hemispherical geometry. The varying expansion rates work in concert to generate the target surface curvature while maintaining structural continuity throughout the transformation process.

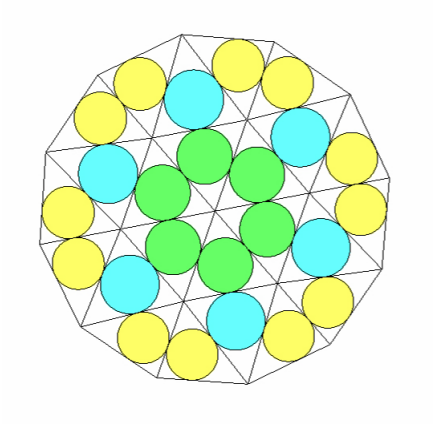

Fig. 12 Circle packing configuration color-coded by radial expansion rates during flat-to-hemisphere transformation. Green, yellow, and blue regions represent decreasing rates of radial expansion required for conformal transformation.

We design compliant mechanisms based on data derived from conformal circle packing analysis. Our approach breaks down the transformation process into two complementary components, as illustrated in Figure 13. First, each mechanism must achieve specific radial expansion targets precisely calculated from our conformal mapping. Second, it must generate controlled curvature while preserving the local geometric relationships that are essential to conformal transformation. To accomplish this dual objective, we strategically position kinematic regions within each mechanism. When an external force is applied, these regions move toward predetermined positions, creating both the required expansion and curvature. The design follows a systematic chain of geometric relationships: the circle packing data defines the target radius, which in turn determines the required curvature while preserving local angles. This curvature requirement establishes the necessary bending rate of the compliant mechanism, which we achieve by precisely controlling the movement of the kinematic regions through applied forces. This integrated approach ensures that each mechanism can achieve both its prescribed radius and curvature targets while maintaining conformal properties and structural integrity throughout the transformation process.

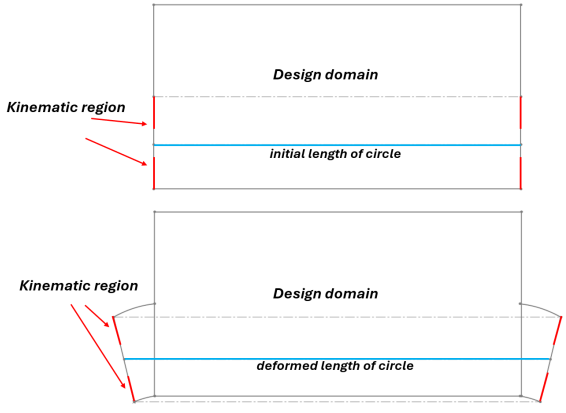

Fig. 13 IDEA OF DESIGNING MORPHABLE SURFACES STRUCTURE BY USING TOPOLOGY OPTIMIZATION.

This method integrates kinematic control with structural compliance to enable precise geometric transformations.

4 SHAPE AND TOPOLOGY OPTIMIZATION OF COMPLIANT MECHANISM

4.1 Conventional Level Set Method. Topology optimization utilizes algorithms to optimize material distribution within a predefined design domain, considering specified objective functions, constraints, and boundary conditions. In recent years, topology optimization has garnered increasing popularity and attention within engineering design circles. Its scope has expanded significantly to address a wide array of challenges involving multiphysics coupling, spanning electromagnetics, thermodynamics, acoustics, solid mechanics, and fluid mechanics, among others.

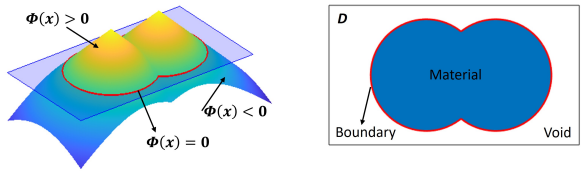

Fig. 14 A SCHEMATIC OF THE LEVEL SET REPRESENTATION.

The level set method, devised by S. Osher and J.A. Sethian, employs a high-dimensional function to represent the 2-D contour implicitly. Pioneered by Sethian and Wiegmann [46] and further refined by Wang [22,47] and Allaire [18], this method has emerged as a promising approach for shape and topology optimization. It ensures a clear boundary between phases without a grey region, significantly enhancing precision and optimization accuracy. In this framework, the structural boundary is implicitly represented as the 2-D contour of a level set function with one higher dimension. Implicitly embedded within the level set function $\Phi(\mathbf{x}, t)$, as shown in Figure 14. Its implicit function representation avoids issues such as checkerboarding and achieves high stability through proper reinitialization and updating schemes to maintain numerical stability. Depending on the sign of the level set function, the design domain can be partitioned into three distinct regions, representing the material, the interface, and the void, respectively, as follows:

$$\begin{cases} \Phi(\mathbf{x}, t) > 0, & x \in \Omega, & \text{Material} \\ \Phi(\mathbf{x}, t) = 0, & x \in \partial\Omega, & \text{Boundary} \\ \Phi(\mathbf{x}, t) < 0, & x \in D/\Omega, & \text{Void} \end{cases} \tag{4}$$

where D denotes the design domain. The evolution of the boundary dynamics is governed by the Hamilton-Jacobi equation:

$$\frac{\partial \Phi(\mathbf{x}, t)}{\partial t} - V_n \cdot |\nabla \Phi(\mathbf{x}, t)| = 0, \tag{5}$$

The normal velocity field V_n can be determined through shape sensitivity analysis. Solving the Hamilton-Jacobi equation outlined above enables updating the normal velocity field, which subsequently governs the evolution of the structural boundary. For details of the classical level set method, please be referred to [19,48,49].

4.2 Problem Formulation. The objective of the topology optimization problem for the single-piece compliant actuator is twofold: (1) kinematic performance, minimizing the discrepancy between the target and the actual deformation of the actuator, and (2) load-carrying capability, maximizing structural stiffness while maintaining a prescribed volume fraction. The problem can be mathematically formulated as follows:

$$
\begin{aligned}
\text{Minimize:} \quad & J = \omega_1 \left(\int_\Omega \varepsilon_{ij}(\boldsymbol{u}) E_{ijkl} \varepsilon_{kl}(\boldsymbol{u}) \, \mathrm{d}\Omega \right) \\
& + \omega_2 \left(\int_\Omega k |\boldsymbol{u} - \boldsymbol{u}_0|^\alpha \, \mathrm{d}\Omega \right)^{\frac{1}{\alpha}}, \\
& \alpha = 2 \\
\text{Subject to:} \quad & a(\boldsymbol{u}, \boldsymbol{v}) = l(\boldsymbol{v}), \quad \forall \mathbf{v} \in U \\
& V(\Omega) = V^*.
\end{aligned} \tag{6}
$$

where u is the state variable (displacement) in the admissible displacement space; Ω is the design variable which is the shape of the material region in the design domain; D represents the design domain; ε_{ij} is the strain tensor; E_{ijkl} is the elasticity tensor; u_0 is the target displacement; k is a weighting factor; ω_1 and ω_2 are weighting coefficients for the stiffness and displacement objectives, respectively; $a(u, v)$ and $l(v)$ are the energy bilinear form and the load linear form, respectively; U is the space of admissible displacements; V^* is the prescribed volume fraction.

The first term in the objective functional J represents the structural stiffness, while the second term measures the discrepancy between the actual and target displacements using an L^α-norm. The parameter α is set to 2, resulting in a quadratic penalty for deviations from the target displacement.

The constraint $a(u, v) = l(v)$ ensures that the displacement field satisfies the governing equations of linear elasticity. The volume constraint $V(\Omega) = \int_\Omega H(\phi) d\Omega = V^*$. limits the amount of material that can be used in the design. k is a region indicator, which equals 1 inside a specific region, and 0 outside [18].

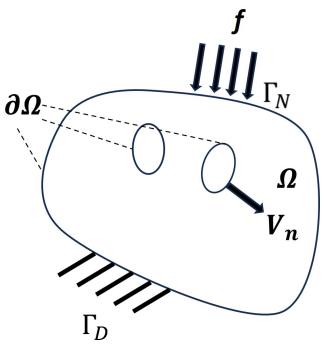

Fig. 15 A SCHEMATIC OF GENERAL BOUNDARY CONDITION.

4.3 Shape Sensitivity Analysis. The topology optimization problem for the single-piece soft actuator can be formulated as a PDE-constrained optimization problem. To solve this problem, the Lagrange multipliers method is utilized to transform the PDE-constrained problem into an unconstrained optimization problem. This is achieved by defining the Lagrangian functional L as follows, which integrates the objective function and governing equation with a Lagrange multiplier λ.

$$
L = J + \lambda(a(\boldsymbol{u}, \boldsymbol{v}) - l(\boldsymbol{v})), \tag{7}
$$

where J is the objective functional, $a(\boldsymbol{u}, \boldsymbol{v})$ represents the weak form of the governing equations, and $l(\boldsymbol{v})$) is the load functional.

4.3.1 Derivation of Adjoint Equation:. To derive the adjoint equation, we take the variation of the Lagrangian functional L with respect to the state variable $\mathbf{u}$ and the Lagrange multiplier λ:

$$
\delta L = \delta J + \lambda(\delta a(u, v) - \delta l(v)) \tag{8}
$$

Setting $\delta L = 0$ leads to the adjoint equation:

$$
a(u', v) = -\frac{\delta J}{\delta u} \tag{9}
$$

where v is the adjoint variable and u' is the test function.

As for this problem, the total derivative of the objective function and governing equation is as follows:

$$
\frac{DL}{Dt} = \frac{DJ}{Dt} + \frac{Da(\boldsymbol{u}, \boldsymbol{v})}{Dt} - \frac{Dl(\boldsymbol{v})}{Dt} \tag{10}
$$

The material time derivative of the objective function is formulated as :

$$
\begin{aligned}
& \frac{DL}{Dt} = \frac{\partial J}{\partial t} + \frac{\partial J}{\partial \Omega} \\
& \frac{\partial J}{\partial t} = 2\omega_1 \left(\int_\Omega \varepsilon_{ij}(\boldsymbol{u}') E_{ijkl} \varepsilon_{kl}(\boldsymbol{u}) \, \mathrm{d}\Omega \right) \\
& + \omega_2 \left(\int_\Omega k |\boldsymbol{u} - \boldsymbol{u}_0|^2 \, \mathrm{d}\Omega \right)^{-\frac{1}{2}} \cdot \int_\Omega k(\boldsymbol{u} - \boldsymbol{u}_0) \cdot \boldsymbol{u}' \, \mathrm{d}\Omega \\
& \frac{\partial J}{\partial \Omega} = \omega_1 \left(\int_\Omega \varepsilon_{ij}(\boldsymbol{u}) E_{ijkl} \varepsilon_{kl}(\boldsymbol{u}) \boldsymbol{V}_n \, \mathrm{d}s \right) \\
& + \frac{\omega_2}{2} \left(\int_\Omega k |\boldsymbol{u} - \boldsymbol{u}_0|^2 \, \mathrm{d}\Omega \right)^{-\frac{1}{2}} \cdot \int_{\partial\Omega} k(\boldsymbol{u} - \boldsymbol{u}_0)^2 \cdot \boldsymbol{V}_n \, \mathrm{d}s.
\end{aligned} \tag{11}
$$

The material time derivative of the internal energy can be expressed as:

$$
\begin{aligned}
& \frac{Da(\boldsymbol{u}, \boldsymbol{v})}{Dt} = \frac{\partial a(\boldsymbol{u}, \boldsymbol{v})}{\partial t} + \frac{\partial a(\boldsymbol{u}, \boldsymbol{v})}{\partial \Omega}, \\
& \frac{\partial a(\boldsymbol{u}, \boldsymbol{v})}{\partial t} = \int_\Omega \varepsilon_{ij}(\boldsymbol{u}') E_{ijkl} \varepsilon_{kl}(\boldsymbol{v}) \, \mathrm{d}\Omega \\
& + \int_\Omega \varepsilon_{ij}(\boldsymbol{u}) E_{ijkl} \varepsilon_{kl}(\boldsymbol{v}') \, \mathrm{d}\Omega, \\
& \frac{\partial a(\boldsymbol{u}, \boldsymbol{v})}{\partial \Omega} = \int_\Omega \varepsilon_{ij}(\boldsymbol{u}) E_{ijkl} \varepsilon_{kl}(\boldsymbol{v}) \boldsymbol{V}_n \, \mathrm{d}s.
\end{aligned} \tag{12}
$$

The material time derivative of the external energy can be expressed as:

$$
\begin{aligned}
& \frac{Dl(\boldsymbol{v})}{Dt} = \frac{\partial l(\boldsymbol{v})}{\partial t} + \frac{\partial l(\boldsymbol{v})}{\partial \Omega} \\
& = \int_\Omega \boldsymbol{g} \cdot \boldsymbol{v}' \mathrm{d}\Omega + \int_{\Gamma_N} \boldsymbol{f} \cdot \boldsymbol{v}' \, \mathrm{d}\Gamma_N \\
& + \int_{\partial\Omega} \boldsymbol{g} \cdot \boldsymbol{v} \boldsymbol{V}_n \mathrm{d}s \\
& + \int_{\partial\Omega} [\frac{\partial(\boldsymbol{f} \cdot \boldsymbol{v})}{\partial n} + k(\boldsymbol{f} \cdot \boldsymbol{v})] \boldsymbol{V}_n \mathrm{d}s,
\end{aligned} \tag{13}
$$

where $\boldsymbol{v}$ is the adjoint displacement field.
Here, the total derivative can be rewritten as:

$$\begin{aligned}\frac{DL}{Dt} &= 2\omega_1\left(\int_\Omega \varepsilon_{ij}(\boldsymbol{u}')E_{ijkl}\varepsilon_{kl}(\boldsymbol{u})\,\mathrm{d}\Omega\right)\\ &+\omega_2\left(\int_\Omega k|\boldsymbol{u}-\boldsymbol{u}_0|^2\,\mathrm{d}\Omega\right)^{-\frac{1}{2}}\cdot\int_\Omega k(\boldsymbol{u}-\boldsymbol{u}_0)\cdot\boldsymbol{u}'\,\mathrm{d}\Omega\\ &+\omega_1\left(\int_\Omega \varepsilon_{ij}(\boldsymbol{u})E_{ijkl}\varepsilon_{kl}(\boldsymbol{u})\boldsymbol{V}_n\,\mathrm{d}s\right)\\ &+\frac{\omega_2}{2}\left(\int_\Omega k|\boldsymbol{u}-\boldsymbol{u}_0|^2\,\mathrm{d}\Omega\right)^{-\frac{1}{2}}\cdot\int_{\partial\Omega}k(\boldsymbol{u}-\boldsymbol{u}_0)^2\cdot\boldsymbol{V}_n\,\mathrm{d}s\\ &+\int_\Omega \varepsilon_{ij}(\boldsymbol{u}')E_{ijkl}\varepsilon_{kl}(\boldsymbol{v})\,\mathrm{d}\Omega+\int_\Omega \varepsilon_{ij}(\boldsymbol{u})E_{ijkl}\varepsilon_{kl}(\boldsymbol{v}')\,\mathrm{d}\Omega\\ &+\int_\Omega \varepsilon_{ij}(\boldsymbol{u})E_{ijkl}\varepsilon_{kl}(\boldsymbol{v})\boldsymbol{V}_n\,\mathrm{d}s-\int_\Omega \boldsymbol{g}\cdot\boldsymbol{v}'\mathrm{d}\Omega\\ &-\int_{\Gamma_N}\boldsymbol{f}\cdot\boldsymbol{v}'\,\mathrm{d}\Gamma_N-\int_{\partial\Omega}\boldsymbol{g}\cdot\boldsymbol{v}\boldsymbol{V}_n\mathrm{d}s\\ &-\int_{\partial\Omega}\left[\frac{\partial(\boldsymbol{f}\cdot\boldsymbol{v})}{\partial n}+k(\boldsymbol{f}\cdot\boldsymbol{v})\right]\boldsymbol{V}_n\mathrm{d}s\end{aligned}\tag{14}$$

Because $\boldsymbol{v}$ is an arbitrary function in the governing equation $a(\boldsymbol{u},\boldsymbol{v})-l(\boldsymbol{v})=0$, by replacing $\boldsymbol{v}$ with $\boldsymbol{v}$' in the governing equation, we can get $a(\boldsymbol{u},\boldsymbol{v}')-l(\boldsymbol{v}')=0$, that is,

$$\int_\Omega \varepsilon_{ij}(\boldsymbol{u})E_{ijkl}\varepsilon_{kl}(\boldsymbol{v}')\,\mathrm{d}\Omega-\int_\Omega \boldsymbol{g}\cdot\boldsymbol{v}'\mathrm{d}\Omega-\int_{\Gamma_N}\boldsymbol{f}\cdot\boldsymbol{v}'\,\mathrm{d}\Gamma_N=0.\tag{15}$$

By simplifying equation 14 with equation 15 and collecting all the terms containing $\boldsymbol{u}$', we can construct the adjoint equation as follows:

$$\begin{aligned}&2\omega_1\left(\int_\Omega \varepsilon_{ij}(\boldsymbol{u}')E_{ijkl}\varepsilon_{kl}(\boldsymbol{u})\,\mathrm{d}\Omega\right)\\ &+\omega_2\left(\int_\Omega k|\boldsymbol{u}-\boldsymbol{u}_0|^2\,\mathrm{d}\Omega\right)^{-\frac{1}{2}}\cdot\int_\Omega k(\boldsymbol{u}-\boldsymbol{u}_0)\cdot\boldsymbol{u}'\,\mathrm{d}\Omega\\ &+\int_\Omega \varepsilon_{ij}(\boldsymbol{u}')E_{ijkl}\varepsilon_{kl}(\boldsymbol{v})\,\mathrm{d}\Omega=0\end{aligned}\tag{16}$$

Let $D_0=(\int_\Omega k|\boldsymbol{u}-\boldsymbol{u}_0|^2\,\mathrm{d}\Omega)^{-\frac{1}{2}}$, then, following [48], we can write the above equation as follows:

$$\begin{aligned}&\int_\Omega \varepsilon_{ij}(\boldsymbol{u}')E_{ijkl}\varepsilon_{kl}(\boldsymbol{v})\,\mathrm{d}\Omega=\\ &-\omega_2D_0\cdot\int_\Omega k(\boldsymbol{u}-\boldsymbol{u}_0)\cdot\boldsymbol{u}'\,\mathrm{d}\Omega\\ &-2\omega_1\left(\int_\Omega \varepsilon_{ij}(\boldsymbol{u}')E_{ijkl}\varepsilon_{kl}(\boldsymbol{u})\,\mathrm{d}\Omega\right).\end{aligned}\tag{17}$$

Since $\boldsymbol{v}$ is an arbitrary function in the governing equation $a(\boldsymbol{u},\boldsymbol{v})-l(\boldsymbol{v})=0$, by replacing $\boldsymbol{v}$ with $\boldsymbol{u}$' in the governing equation, we can get:

$$\int_\Omega \varepsilon_{ij}(\boldsymbol{u}')E_{ijkl}\varepsilon_{kl}(\boldsymbol{u})\,\mathrm{d}\Omega=\int_\Omega \boldsymbol{g}\cdot\boldsymbol{u}'\,\mathrm{d}\Omega+\int_{\Gamma_N}\boldsymbol{f}\cdot\boldsymbol{u}'\,\mathrm{d}\Gamma_N,\tag{18}$$

Substituting equation 18 into the equation 17, the equation 17 can be rewritten as:

$$\begin{aligned}&\int_\Omega \varepsilon_{ij}(\boldsymbol{u}')E_{ijkl}\varepsilon_{kl}(\boldsymbol{v})\,\mathrm{d}\Omega=\\ &-\omega_2D_0\cdot\int_\Omega k(\boldsymbol{u}-\boldsymbol{u}_0)\cdot\boldsymbol{u}'\,\mathrm{d}\Omega-2\omega_1\int_\Omega \boldsymbol{g}\cdot\boldsymbol{u}'\,\mathrm{d}\Omega\\ &-2\omega_1\int_{\Gamma_N}\boldsymbol{f}\cdot\boldsymbol{u}'\,\mathrm{d}\Gamma_N.\end{aligned}\tag{19}$$

Then, equation 19 can be rewritten as:

$$\begin{aligned}&\int_\Omega \varepsilon_{ij}(\boldsymbol{u}')E_{ijkl}\varepsilon_{kl}(\boldsymbol{v})\,\mathrm{d}\Omega=\\ &\int_\Omega(-\omega_2D_0\cdot k(\boldsymbol{u}-\boldsymbol{u}_0)-2\omega_1 g)\cdot\boldsymbol{u}'\,\mathrm{d}\Omega+\\ &\int_{\Gamma_N}(-2\omega_1\cdot\boldsymbol{f})\cdot\boldsymbol{u}'\,\mathrm{d}\Gamma_N.\end{aligned}\tag{20}$$

The strong form of the adjoint solution is as follows:

$$\begin{aligned}-\nabla\cdot\sigma(\boldsymbol{v})&=-\omega_2D_0\cdot k(\boldsymbol{u}-\boldsymbol{u}_0)-2\omega_1\boldsymbol{g},\text{ on }\Omega,\\ \boldsymbol{v}&=0,\text{ on }\Gamma_D,\\ \sigma(\boldsymbol{v})\cdot\boldsymbol{n}&=-2\omega_1\cdot\boldsymbol{f},\text{ on }\Gamma_N.\end{aligned}\tag{21}$$

4.3.2 Construction of Design Velocity:. Once the adjoint equation is solved, the design velocity V_n can be calculated using the following expressions. In this work, the body force $\mathbf{g}$ is not considered in the problem:

$$\begin{aligned}&\omega_1\left(\int_{\partial\Omega}\varepsilon_{ij}(\boldsymbol{u})E_{ijkl}\varepsilon_{kl}(\boldsymbol{u})\boldsymbol{V}_n\,\mathrm{d}s\right)\\ &+\frac{\omega_2}{2}\left(\int_\Omega k|\boldsymbol{u}-\boldsymbol{u}_0|^2\,\mathrm{d}\Omega\right)^{-\frac{1}{2}}\cdot\int_{\partial\Omega}k(\boldsymbol{u}-\boldsymbol{u}_0)^2\cdot\boldsymbol{V}_n\,\mathrm{d}s\\ &+\int_{\partial\Omega}\varepsilon_{ij}(\boldsymbol{u})E_{ijkl}\varepsilon_{kl}(\boldsymbol{v})\boldsymbol{V}_n\,\mathrm{d}s\end{aligned}\tag{22}$$

With the steepest descent method, the normal design velocity can be constructed as

$$\begin{aligned}V_{n1}&=-\omega_1\varepsilon_{ij}(\boldsymbol{u})E_{ijkl}\varepsilon_{kl}(\boldsymbol{u})\\ V_{n2}&=-\frac{\omega_2}{2}D_0k(\boldsymbol{u}-\boldsymbol{u}_0)^2\\ V_{n3}&=-\varepsilon_{ij}(\boldsymbol{u})E_{ijkl}\varepsilon_{kl}(\boldsymbol{v})\end{aligned}\tag{23}$$

The total design velocity V_n is then obtained by summing these three components:

$$V_n = -\omega_1 \varepsilon_{ij}(\boldsymbol{u}) E_{ijkl} \varepsilon_{kl}(\boldsymbol{u}) - \frac{\omega_2}{2} D_0 k(\boldsymbol{u} - \boldsymbol{u}_0)^2 - \varepsilon_{ij}(\boldsymbol{u}) E_{ijkl} \varepsilon_{kl}(\boldsymbol{v}) \tag{24}$$

This design velocity is used to evolve the structural boundary and optimize the topology of the compliant actuator.

5 NUMERICAL EXAMPLES

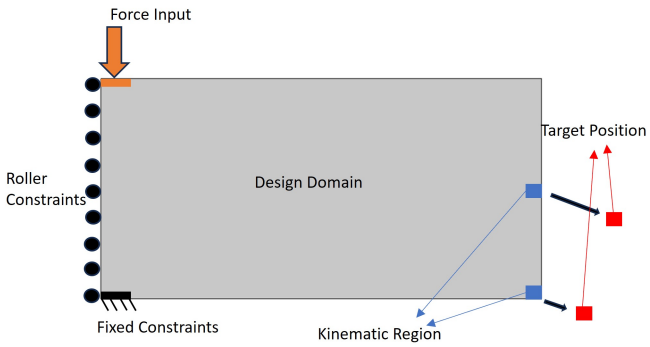

Fig. 16 BOUNDARY CONDITIONS OF THE SINGLE-PIECE ACTUATOR

5.1 Numerical Example I: Topology Optimization of Single-piece compliant actuator. This example is to find the optimum design of the single-piece compliant actuator. Compliant mechanisms can be evaluated based on several criteria, including geometric advantages, mechanical advantages, energy efficiency, target diaplacement [17,50], and kinematic precision [51]. In this design example, target displacement was considered by incorporating the least square error between the target and actual displacement into the objective function. As Figure 16 shows, the boundary conditions of the single-piece actuator are the Input force at the top left, roller constraints at the left edge, and fixed constraints at the bottom left. Two blue squares indicate the kinematic region, and the two red squares indicate the target position the kinematic region tries to approach. The target position is determined by the circle packing algorithms. Based on the data generated, we can find the corresponding radii and the curvature target of every single circular actuator can be found from the overall radii. The window factor k is zero except in the blue zone, where it is equal to 1. The force applied is 3 Newton. The material used in this example is a dummy material with Young's modulus E = 1000 Pa, the Poisson's ratio is given by 0.3, and the density is 1. The weighting factor of this topology optimization problem is w_1 = 0.0042, w_2 = 0.9958.

The entire design domain is discretized into 100 50 grids. Both constituent materials are constrained to occupy 30 percent of the total volume. Figure 17 depicts the convergence curve of the optimization process and the history of design evolution. The optimization process involves a total of 2000 iterations. The convergence plot shows that the objective function stabilizes after approximately 300 iterations and converges after 500 iterations. The computational cost in topology optimization primarily arises from two finite element analyses (FEA) performed at each iteration: one for the forward simulation and another for the adjoint simulation. Both analyses are computationally intensive. Key factors that influence computation time include mesh resolution, the number of design variables, and the complexity of the physics model. In this example, variations in boundary and initial conditions have minimal impact on computational time. The mesh size, number of

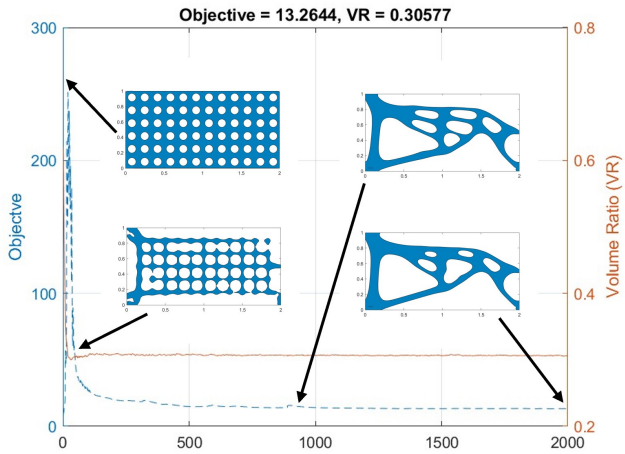

Fig. 17 THE TOPOLOGY OPTIMIZATION CONVERGENCE PLOT.

design variables, and the physical model—governed by the linear elasticity equation—remain unchanged, ensuring consistent computational requirements.

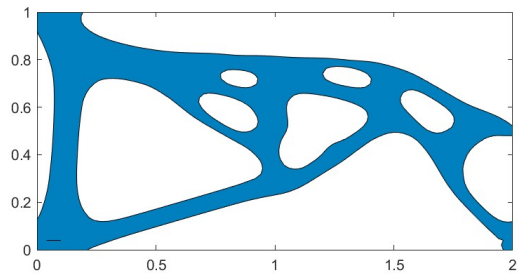

Fig. 18 FINAL RESULT OF THE TOPOLOGY-OPTIMIZED COMPLIANT ACTUATOR.

Following 2000 iterations of evolution, the optimization outcome is depicted in Figure 18. Material regions are represented in blue, while void regions are displayed in white. In this numerical example, finite element analysis is carried out to verify the optimization results, with boundary conditions applied to the optimized outcome. The verification results are illustrated in Figure 20. A downward force of 3 Newton is applied at the top left, and the kinematic region converges toward the target position. The final volume ratio is 30 percent.

The single-piece soft actuator successfully meets the design criteria following verification. Utilizing symmetry, the single-circular actuator is constructed from the circular pattern of single-piece actuators. Six single-piece actuators are assembled to form one circular actuator. The number of spokes in the circular actuators is not strictly constrained. Designs with both six and eight spokes have been explored, as illustrated in Figure 19 and 21. Figure 21 depicts the single circular actuator and its verification, conducted via finite element analysis. A force is applied to the top of the circular actuator, resulting in the bending and expansion of the entire structure according to the designed curvature and radius. In future physical experiments, the force could be generated by a motor or

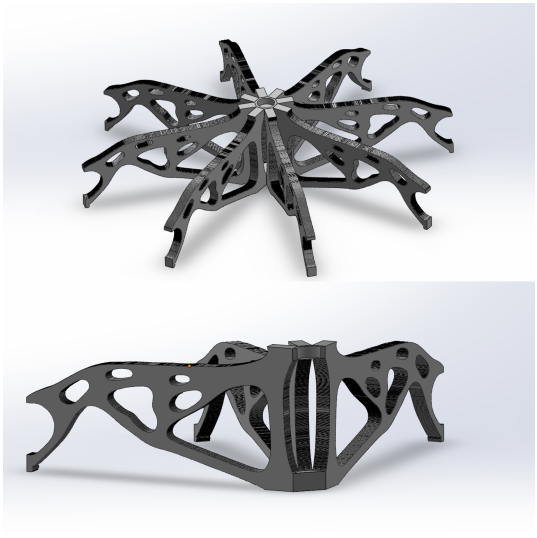

Fig. 19 SECTION VIEW AND CIRCULAR ASSEMBLED

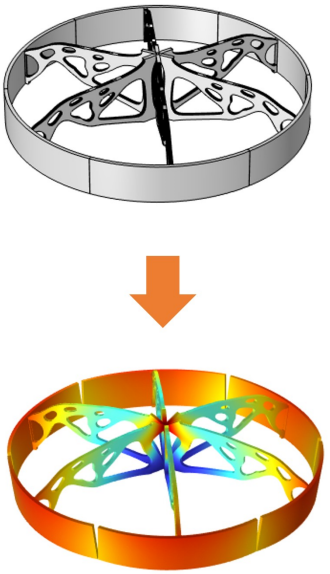

Fig. 21 NUMERICAL VERIFICATION OF THE BEHAVIOR of A CIRCULAR COMPLIANT ACTUATOR ASSEMBLY.

similar device.

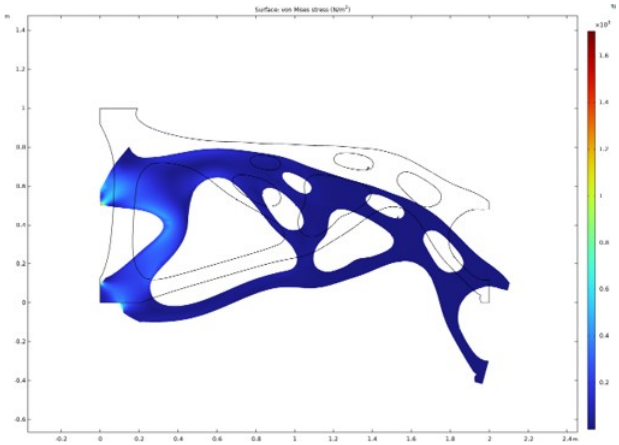

Fig. 20 NUMERICAL VALIDATION OF THE MORPHING BEHAVIOR OF THE COMPLIANT ACTUATOR DESIGNED USING TOPOLOGY OPTIMIZATION.

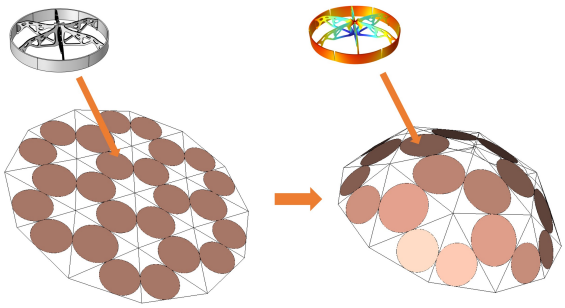

Fig. 22 SINGLE CIRCULAR COMPLIANT ACTUATOR CORRESPONDING TO CIRCLE PACKING STRUCTURES.

5.2 System Analysis of The Entire Circular Packing System in Example I. The complete morphable surface structure comprises 24 single circular actuators, each constructed from 6 single-piece actuators. Once assembled, as depicted in Figure 22, the curvature and radius of the entire structure are validated against the graph in Figure 23, generated through circle packing algorithms. The verification of the single-piece actuator was conducted using finite element analysis. Similarly, the single circular actuator assembled from the single-piece actuators underwent verification via finite element analysis. Once the single circular actuator is verified, it can be integrated into the overall morphable surface structure.

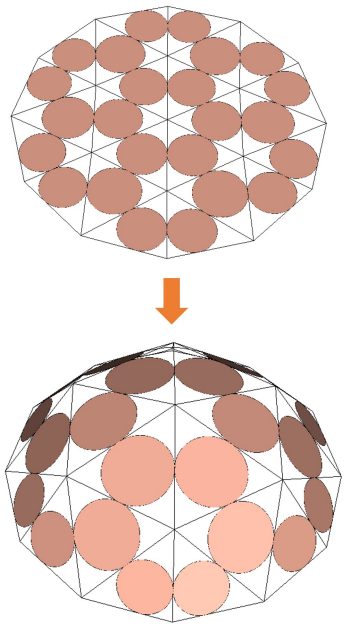

Fig. 23 TRANSFORMATION OF A FLAT SURFACE INTO A COMPLEX 3D GEOMETRY THROUGH CIRCLE PACKING-BASED MORPHABLE DESIGN.

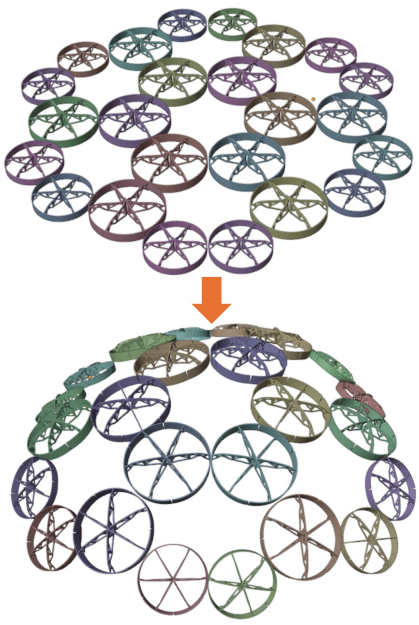

Fig. 24 SIMULATION OF THE PHYSICAL BEHAVIORS of THE CIRCLE-PACKING MORPHABLE SURFACES STRUCTURE.

5.3 Numerical Example II: Stretch From a Unit Cube To A Trapezohedron. In the first example, the structure morphs from a flat panel to a hemisphere [52]. The second case study demonstrates a transition from a unit cube to a trapezohedron, as illustrated in Figure 25 and 26. Figure 25 depicts the underlying morphing structure's spatial representation, while Figure 26 highlights the corresponding circle packing transition from a unit cube to a trapezohedron. As in the first example, the design objective is to create a single-piece mechanism through topology optimization to achieve the target kinematics and positional requirements. The target position in the second example differs from the first, resulting in distinct computational outcomes. The boundary conditions for this single-piece actuator include an input force of 4 N applied at the top left, roller constraints at the top left, and a fixed constraint at the bottom left. The material properties used in this study are Young's modulus E=1500 Pa, Poisson's ratio v=0.3, and density ρ=1. The weighting factors for the topology optimization problem are w_1 = 0.005, w_2 = 0.995. The convergence plot is presented in Figure 28. The optimized single-piece mechanism, consisting of a circular revolved structure with six spokes, is shown in Figure 27. Verification results, shown in Figure 29, confirm that the soft actuator meets the design criteria. When a force is applied to the top of the circular actuator, the structure bends and expands, achieving the designed curvature and radius, as demonstrated in Figure 31.

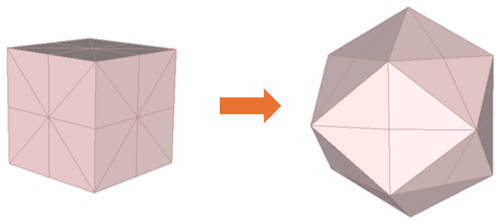

Fig. 25 THE UNDERLYING SPACE OF A UNIT CUBE TO A TRAPEZOHEDRON.

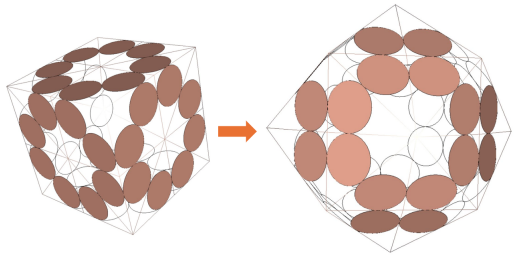

Fig. 26 THE CIRCLE PACKING FROM A UNIT CUBE TO A TRAPEZOHEDRON.

	Initial Length	Target Length After Deformation	Actual Length After Deformation	Error
Example 1	2	2.226	2.180	2.058%
Example 2	2	2.239	2.172	3.001%

Table 1 Error calculation of the two numerical examples.

5.4 System Analysis of the Transformation from a Unit Cube to a Trapezohedron. The transformation from a unit cube

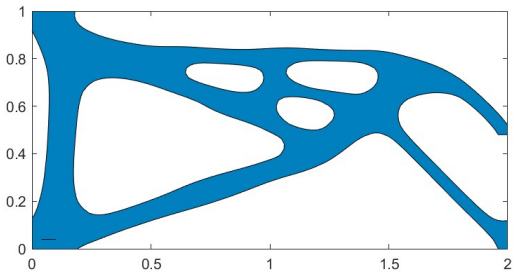

Fig. 27 FINAL RESULT OF THE TOPOLOGY-OPTIMIZED COMPLIANT ACTUATOR.

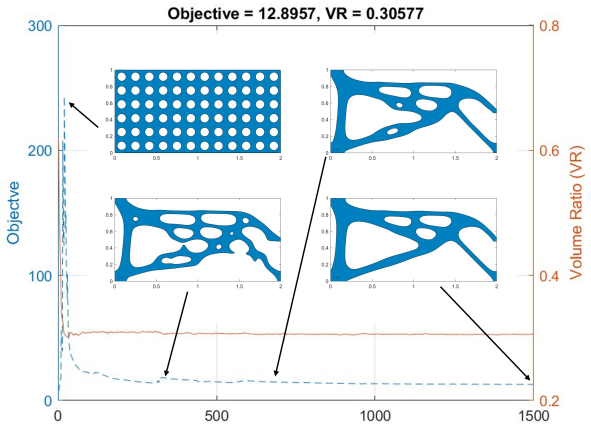

Fig. 28 THE TOPOLOGY OPTIMIZATION CONVERGENCE PLOT.

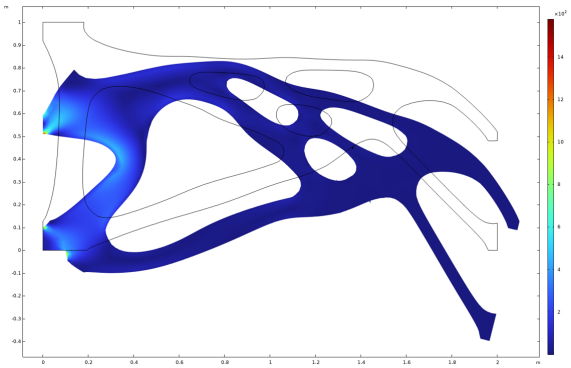

Fig. 29 NUMERICAL VALIDATION OF THE MORPHING BEHAVIOR OF THE COMPLIANT ACTUATOR DESIGNED USING TOPOLOGY OPTIMIZATION.

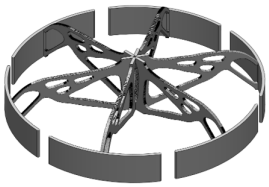

Fig. 30 ASSEMBLED OF SINGLE CIRCULAR MECHANISM .

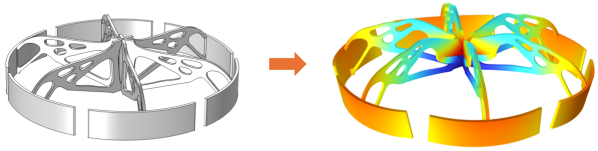

Fig. 31 NUMERICAL VERIFICATION OF THE BEHAVIOR of A CIRCULAR COMPLIANT ACTUATOR ASSEMBLY.

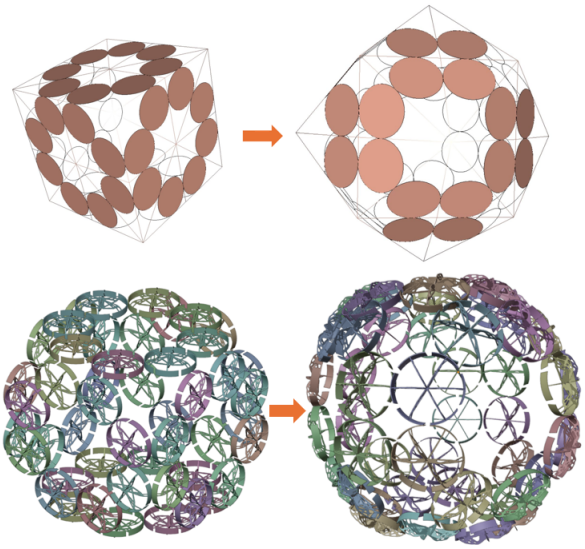

Fig. 32 TRANSFORMATION OF A UNIT CUBE INTO A TRAPEZOHEDRON THROUGH CIRCLE PACKING-BASED MORPHABLE DESIGN.

to a trapezohedron in this design example involves a total of 48 single circular mechanisms. Since the structure transitions uniformly from a unit cube to a trapezohedron, the expansion and overall morphing behavior of each single circular mechanism remain consistent throughout the structure.

As illustrated in Figure 32, the initial and final circle packs of the unit cube and trapezohedron configurations were replaced with single circular mechanisms in their respective initial and deformed states. Each single circular actuator was individually verified through finite element analysis to ensure its performance. Once validated, these actuators were seamlessly integrated into the overall morphable surface structure, enabling precise and reliable transformation.

6 DISCUSSIONS AND CONCLUSIONS

This paper presents a new computational framework for designing morphable surface structures. The core contribution is the integrated framework that synergistically combines circle packing and topology optimization. This unique combination enables the generation of optimized compliant actuators capable of dynamically adjusting their radius and curvature to conform to target shapes. The concept of control is implicitly embedded within the design of these actuators; by predefining specific radii and curvatures derived from the circle packing representation, the framework facilitates coordinated deformation across the entire structure. This integrated approach surpasses conventional methods by simultaneously considering both the local geometry of individual components and the global morphology of the system, ultimately enabling coordinated control over the morphable surface.

While traditional circle packing helps determine the radii of circles in each configuration, it overlooks critical factors such as the thickness and curvature of these circles, which are essential in mechanical design. We address this shortcoming by introducing a two-layer circular mechanism that permits both radial expansion and adjustments to the overall curvature. This innovative mechanism not only allows for vertical and horizontal adjustments to the position of the specific output region but also enables manipulation of the output region's orientation, providing a comprehensive solution that overcomes the limitations inherent in traditional circle packing approaches.

The design of individual circular mechanisms employs a dual-transformation approach: it simultaneously changes the radius of the circle while inducing controlled bending in the structure. When force is applied, it causes paired kinematic regions to move toward positions predetermined by conformal mapping, enabling both radial expansion and curvature generation for each circular mechanism to achieve its target configuration. To verify this approach, we conducted error analysis across two numerical examples, as shown in Table 1, measuring the length of each compliant mechanism (which corresponds directly to the radius of its circular mechanism). Starting from an initial length of 2 units in both examples, we compared the target and actual deformation lengths. In the first example, the mechanism achieved a final length of 2.180 units compared to the target of 2.226 units, representing a deviation of 2.058%. The second example showed similar precision, with the mechanism reaching 2.172 units versus a target of 2.239 units, resulting in a 3.001% error. These small margins of error demonstrate the high precision of our design methodology in achieving both the desired radial expansion and curvature transformation.

Current state-of-the-art methods for designing morphing structures utilize a variety of approaches, including auxetic metamaterials, rigid-body mechanisms relying on kinematics, and shape memory polymers acting as smart materials. While effective, these methods can be complemented by our approach, which couples circle packing theory with topology optimization. Although the computational time required for the topology optimization process is relatively long compared to other design methodologies, this combination leverages the strengths of both approaches. Circle packing theory ensures geometric accuracy in representing the desired shapes, while topology optimization facilitates the discovery of innovative design solutions, automates the design process, and enhances overall performance. This integrated framework ultimately enables the creation of advanced morphing surface structures with improved functionality and efficiency, pushing the boundaries beyond the capabilities of existing methods.

The morphing behavior of a single circular actuator is initiated by a downward input force at its center. Currently, our simulations assume linear elasticity for simplicity, though we recognize that the soft material used actually exhibits nonlinear elastic behavior. When integrated into the overall structure, these individual actuators are assembled and reconfigured from a flat panel into a half-spherical shape. This process highlights some limitations of our current method, which are rooted in geometric constraints, material properties, physical limitations, and control challenges. Geometrically, the underlying circle packing technique is most effective with convex shapes and struggles to accurately represent concave geometries. Material limitations also play a role, particularly when dealing with intricate shapes with significant curvature, as the material's properties can restrict the achievable deformation. The displacement objective function is formulated as a least-squares function, meaning the optimization seeks to minimize the squared difference between the actual and target displacements. However, because this target displacement is treated as a "soft" objective rather than a "hard" constraint, the optimization may not guarantee that the target displacement is exactly achieved. In particular, when working with materials that have high elastic moduli, the physical stiffness of the resulting compliant mechanism may prevent it from reaching the desired displacement magnitude, even if the volume fraction constraint is fully satisfied. The final challenge lies in control: coordinating the transition from individual, optimized mechanisms to a unified, morphable structure presents complexities in terms of system integration.

Future work will tackle these challenges by incorporating material nonlinearity into our analysis, improving the conformal geometry framework to handle a wider range of shapes and geometries, and refining control strategies to enable seamless coordination between individual units and the overall structure. Additionally, we will strive for fully automated simulation, allowing for seamless morphing from a flat panel to a half sphere without manual intervention. Finally, experiments and physical validations will be conducted to corroborate the effectiveness of the proposed approach.

7 ACKNOWLEDGEMENT

This research was supported by grants from the National Science Foundation (CMMI-1762287 and PFI-RP-2213852) and by funding from the Toyota Research Institute of North America (Award 93761).

References

[1] Liu, K., Hacker, F., and Daraio, C., 2021, "Robotic surfaces with reversible, spatiotemporal control for shape morphing and object manipulation," Science Robotics, **6**(53), p. eabf5116.

[2] Chen, Q., Feng, F., Lv, P., and Duan, H., 2022, "Origami spring-inspired shape morphing for flexible robotics," Soft Robotics, **9**(4), pp. 798–806.

[3] Ishida, M., Drotman, D., Shih, B., Hermes, M., Luhar, M., and Tolley, M. T., 2019, "Morphing structure for changing hydrodynamic characteristics of a soft underwater walking robot," IEEE Robotics and Automation Letters, **4**(4), pp. 4163–4169.

[4] Belobaba, P., Cooper, J., Langton, R., and Seabridge, A., 2012, *Morphing aerospace vehicles and structures*, Vol. 57, John Wiley & Sons.

[5] Fasel, U., Keidel, D., Baumann, L., Cavolina, G., Eichenhofer, M., and Ermanni, P., 2020, "Composite additive manufacturing of morphing aerospace structures," Manufacturing Letters, **23**, pp. 85–88.

[6] Bendsøe, M. P. and Sigmund, O., 1999, "Material interpolation schemes in topology optimization," Archive of applied mechanics, **69**, pp. 635–654.

[7] Bendsoe, M. P. and Sigmund, O., 2013, *Topology optimization: theory, methods, and applications*, Springer Science & Business Media.

[8] Sigmund, O. and Bondsgc, M., 2003, "Topology optimization," State-of-the-Art and Future Perspectives, Copenhagen: Technical University of Denmark (DTU).

[9] Luo, Z., Wang, M. Y., Wang, S., and Wei, P., 2008, "A level set-based parameterization method for structural shape and topology optimization," International Journal for Numerical Methods in Engineering, **76**(1), pp. 1–26.

[10] Howell, L. L., Magleby, S. P., Olsen, B. M., and Wiley, J., 2013, *Handbook of compliant mechanisms*, Wiley Online Library.

[11] Smith, S. T., 2000, *Flexures: elements of elastic mechanisms*, Crc Press.

[12] Burns, R., 1966, "Structural permutations of flexible link mechanisms," *Mechanical Engineering*, Vol. 88, ASME-AMER SOC MECHANICAL ENG 345 E 47TH ST, NEW YORK, NY 10017, Paper No. 11, p. 84.

[13] Paros, J., 1965, "Flexure hinges," Machine design, **37**, pp. 151–156.

[14] Bruns, T. E. and Tortorelli, D. A., 2001, "Topology optimization of non-linear elastic structures and compliant mechanisms," Computer methods in applied mechanics and engineering, **190**(26-27), pp. 3443–3459.

[15] Frecker, M., Ananthasuresh, G., Nishiwaki, S., Kikuchi, N., and Kota, S., 1997, "Topological synthesis of compliant mechanisms using multi-criteria optimization," .

[16] Nishiwaki, S., Frecker, M. I., Min, S., and Kikuchi, N., 1998, "Topology optimization of compliant mechanisms using the homogenization method," International journal for numerical methods in engineering, **42**(3), pp. 535–559.

[17] Sigmund, O., 1997, "On the design of compliant mechanisms using topology optimization," Journal of Structural Mechanics, **25**(4), pp. 493–524.

[18] Allaire, G., Jouve, F., and Toader, A.-M., 2004, "Structural optimization using sensitivity analysis and a level-set method," Journal of computational physics, **194**(1), pp. 363–393.

[19] Wang, M. Y., Wang, X., and Guo, D., 2003, "A level set method for structural topology optimization," Computer methods in applied mechanics and engineering, **192**(1-2), pp. 227–246.

[20] Kim, C. J., Kota, S., and Moon, Y.-M., 2006, "An instant center approach toward the conceptual design of compliant mechanisms," .

[21] Wang, H. V., 2005, *A unit cell approach for lightweight structure and compliant mechanism*, Georgia Institute of Technology.

[22] Wang, S. and Wang, M. Y., 2006, "Radial basis functions and level set method for structural topology optimization," International journal for numerical methods in engineering, **65**(12), pp. 2060–2090.

[23] Jiang, L., Chen, S., and Jiao, X., 2018, "Parametric shape and topology optimization: A new level set approach based on cardinal basis functions," International Journal for Numerical Methods in Engineering, **114**(1), pp. 66–87.

[24] Dudek, K. K., Martínez, J. A. I., Ulliac, G., and Kadic, M., 2022, "Micro-scale auxetic hierarchical mechanical metamaterials for shape morphing," Advanced Materials, **34**(14), p. 2110115.

[25] Yao, Y., Luo, Y., Xu, Y., Wang, B., Li, J., Deng, H., and Lu, H., 2018, "Fabrication and characterization of auxetic shape memory composite foams," Composites Part B: Engineering, **152**, pp. 1–7.

[26] Tian, J., Li, M., Han, Z., Chen, Y., Gu, X. D., Ge, Q., and Chen, S., 2022, "Conformal topology optimization of multi-material ferromagnetic soft active structures using an extended level set method," Computer Methods in Applied Mechanics and Engineering, **389**, p. 114394.

[27] Luo, J., Luo, Z., Chen, S., Tong, L., and Wang, M. Y., 2008, "A new level set method for systematic design of hinge-free compliant mechanisms," Computer Methods in Applied Mechanics and Engineering, **198**(2), pp. 318–331.

[28] Tian, J., Zhao, X., Gu, X. D., and Chen, S., 2020, "Designing Ferromagnetic Soft Robots (FerroSoRo) with Level-Set-Based Multiphysics Topology Optimization," *2020 IEEE International Conference on Robotics and Automation (ICRA)*, pp. 10067–10074, doi: 10.1109/ICRA40945.2020.9197457.

[29] Wang, M. Y., Chen, S., Wang, X., and Mei, Y., 2005, "Design of Multimaterial Compliant Mechanisms Using Level-Set Methods," Journal of Mechanical Design, **127**(5), pp. 941–956.

[30] Xu, X., Gu, X. D., and Chen, S., 2022, "Shape and topology optimization of conformal thermal control structures on free-form surfaces: A dimension reduction level set method (DR-LSM)," Computer Methods in Applied Mechanics and Engineering, **398**, p. 115183.

[31] Ye, Q., Guo, Y., Chen, S., Lei, N., and Gu, X. D., 2019, "Topology optimization of conformal structures on manifolds using extended level set methods (X-LSM) and conformal geometry theory," Computer Methods in Applied Mechanics and Engineering, **344**, pp. 164–185.

[32] Xu, X., Gu, X. D., and Chen, S., 2023, "Topology optimization of thermal cloaks in euclidean spaces and manifolds using an extended level set method," International Journal of Heat and Mass Transfer, **202**, p. 123720.

[33] Luo, Z., Chen, L., Yang, J., Zhang, Y., and Abdel-Malek, K., 2005, "Compliant mechanism design using multi-objective topology optimization scheme of continuum structures," Structural and Multidisciplinary Optimization, **30**, pp. 142–154.

[34] Gu, X. D. and Yau, S. T., 2008, "Computational conformal geometry," (No Title).

[35] Gu, D. X., Luo, F., and Yau, S.-T., 2010, "Fundamentals of computational conformal geometry," Mathematics in Computer Science, **4**, pp. 389–429.

[36] Stephenson, K., 2005, *Introduction to circle packing: The theory of discrete analytic functions*, Cambridge University Press.

[37] Chow, B., Chu, S.-C., Glickenstein, D., Guenther, C., Isenberg, J., Ivey, T., Knopf, D., Lu, P., Luo, F., and Ni, L., 2007, *The Ricci flow: techniques and applications*, Vol. 135, American Mathematical Society Providence.

[38] Koebe, P., 1936, *Kontaktprobleme der konformen Abbildung*, Hirzel.

[39] Rodin, B. and Sullivan, D., 1987, "The convergence of circle packings to the Riemann mapping," Journal of Differential Geometry, **26**, pp. 349–360.

[40] Hamilton, R. S., 1988, "The Ricci Flow on Surfaces," *Mathematics and General Relativity*, Contemporary Mathematics, Vol. 71, American Mathematical Society, Providence, RI, Santa Cruz, CA, 1986.

[41] Chow, B. and Luo, F., 2003, "Combinatorial Ricci flows on surfaces," Journal of Differential Geometry, **63**(1), pp. 97–129.

[42] Thurston, W., 1978-1981, *The Geometry and Topology of 3-Manifolds*, Princeton Lecture Notes.

[43] Weyl, H., 1916, "On the Embedding of Abstract Structures into Euclidean Spaces," Annals of Mathematics, **17**(3), pp. 211–239.

[44] Alexandrov, A. D., 1942, "Existence of a convex polyhedron and of a convex surface with a given metric," Matematicheskii Sbornik, New Series, **11**(53), pp. 15–65.

[45] Izmestiev, I. A., 2008, "A Variational Proof of Alexandrov's Convex Cap Theorem," Discrete Comput Geom, **40**, pp. 561–585.

[46] 2000, "Structural Boundary Design via Level Set and Immersed Interface Methods," Journal of Computational Physics, **163**(2), pp. 489–528.

[47] Wang, M. Y. and Wang, X., 2004, ""Color" level sets: a multi-phase method for structural topology optimization with multiple materials," Computer Methods in Applied Mechanics and Engineering, **193**(6), pp. 469–496.

[48] Allaire, G., Jouve, F., and Toader, A.-M., 2004, "Structural optimization using sensitivity analysis and a level-set method," Journal of Computational Physics, **194**(1), pp. 363–393.

[49] Osher, S. and Fedkiw, R. P., 2001, "Level Set Methods: An Overview and Some Recent Results," Journal of Computational Physics, **169**(2), pp. 463–502.

[50] Howell, L. L., 2013, "Compliant mechanisms," *21st Century Kinematics: The 2012 NSF Workshop*, Springer, pp. 189–216.

[51] Gallego, J. A. and Herder, J., 2009, "Synthesis methods in compliant mechanisms: An overview," *International Design Engineering Technical Conferences and Computers and Information in Engineering Conference*, Vol. 49040, pp. 193–214.

[52] Gao, L., Zhu, X., Tanaka, M., Song, Y., Zhou, Y., Gu, X. D., and Chen, S., 2024, "Geometry-Driven Design of Morphable Surface Structures Using Topology Optimization and Circle Packing," *International Design Engineering Technical Conferences and Computers and Information in Engineering Conference*, Vol. 88414, American Society of Mechanical Engineers, p. V007T07A037.